IMA Journal of Applied Mathematics (2018) Page 1 of 25
doi:10.1093/imamat/xxx000

Enhanced sedimentation of elongated plankton in simple flows

W. CLIFTON AND R. N. BEARON*
Department of Mathematical Sciences, University of Liverpool, Liverpool L69 7ZL, UK
*Corresponding author: rbearon@liverpool.ac.uk

M. A. BEES
Department of Mathematics, University of York, York YO10 5DD, UK

[Received on 11 April 2018]

Negatively buoyant phytoplankton play an important role in the sequestration of CO_2 from the atmosphere and are fundamental to the health of the world's fisheries. However, there is still much to discover on transport mechanisms from the upper photosynthetic regions to the deep ocean. In contrast to intuitive expectations that mixing increases plankton residence time in light-rich regions, recent experimental and computational evidence suggests that turbulence can actually enhance sedimentation of negatively buoyant diatoms. Motivated by these studies we dissect the enhanced sedimentation mechanisms using the simplest possible two-dimensional flows, avoiding expensive computations and obfuscation. In particular, we find that in vertical shear, preferential flow alignment and aggregation in down-welling regions both increase sedimentation, whereas horizontal shear reduces the sedimentation due only to alignment. However the magnitude of the shear does not affect the sedimentation rate. In simple vertical Kolmogorov flow elongated particles also have an enhanced sedimentation speed as they spend more time in down-welling regions of the flow with vertically aligned orientation, an effect that increases with the magnitude of shear. An additional feature is identified in horizontal Kolomogorov flow, whereby the impact of shear-dependent sedimentation speed is to cause aggregation in regions of high-shear where the sedimentation speed is minimum. In cellular flow, there is an increase in mean sedimentation speed with aspect ratio and shear strength associated with aggregation in down-welling regions. Furthermore, spatially projected trajectories can intersect and give rise to chaotic dynamics, which is associated with a depletion of particles within so called retention zones.

Keywords: Plankton, diatoms, enhanced sedimentation, aspect ratio, shear flow, buoyancy

1. Introduction

Phytoplankton are photosynthetic micro-organisms that live in aquatic environments. They are critically important in oceanic food webs; forming the base and sustaining all the world's commercially important fisheries, and playing a critical part in the carbon cycle where they act as a biological pump transporting carbon from the atmosphere to the deep ocean. Here, we are motivated by the study of diatoms, an enormously ecologically important group of microscopic phytoplankton that are non-motile, chain-forming, and negatively buoyant. The settling rate of diatoms in quiescent water was established nearly fifty years ago (Smayda, 1970), yet sedimentation in the turbulent upper layers of the ocean where diatoms reside is still open to question. Early observations indicated that diatoms thrive in turbulent flows (Margalef, 1978) and stirring cultures tended to keep cells in suspension. This led to the paradigm in biological oceanography that turbulence can keep cells suspended in sun-lit surface layers. However, more recent experiments have suggested that turbulence can enhance the sedimentation of diatoms

(Ruiz et al., 2004), and this is supported by new numerical simulations of settling diatom chains in turbulence (Ardekani et al., 2017). These new simulations have identified the importance of the chain aspect ratio on sedimentation and, importantly, they provide intimation of the form of a physical mechanism, demanding further study.

To understand the mechanisms for enhanced sedimentation of diatom chains in turbulence, we observe that diatoms are small (individuals are 1 μm and chains are order 100 μm; compared with the Kolmogorov lengthscale in the oceans of hundreds of μm to mm) and only weakly negatively buoyant. Therefore, following Ardekani et al. (2017), the motion of the particles can be well-described by the inertia-less Stokes flow equations (Voth & Soldati, 2017). By studying simple imposed flow fields, we can identify in isolation mechanisms that impact a particle's trajectory in the flow and hence the resultant sedimentation speed.

The behaviour of particles in a given flow has been studied in a variety of contexts. Of particular relevance to this study is the classical work by Jeffery (1922) who established how neutrally buoyant particles behave in uniform shear flow. In particular, ellipsoids undergo periodic motion with non-uniform rotation rate, with the result that for prolate ellipsoids and rods, the time spent aligned with the flow increases as a function of aspect ratio. Also of relevance are the studies of slender fibres sedimenting in quiescent flow; it has been shown both experimentally and numerically that the mean sedimentation speed is higher for a dilute suspension than the settling rate of an isolated fibre (see the reviews by Guazzelli & Hinch, 2011; Voth & Soldati, 2017). Typically in those studies the flow field generated through hydrodynamic interactions results in a non-uniform spatial distribution of particles, leading to alignment of particles with the vertical. In a numerical study by Siewert et al. (2014) on the settling of inertial non-spherical particles (particularly ice crystals) in decaying isotropic turbulence results support those of earlier studies for spheres (Wang & Maxey, 1993): preferential orientation relative to the direction of gravity and with agreement of time scales for particles and eddies, particles preferentially accumulate in down-welling regions. However, studies of the settling of isolated anisotropic particles in simple external flows are few. Mallier & Maxey (1991) and Shin & Maxey (1997) explored the dynamics of settling particles in cellular flows in relation to Stommel retention zones (Stommel, 1949), demonstrating that circulation induced suspension still occurs for non-spherical particles, albeit in a reduced region, and that chaotic motion can occur. Such dynamics are backed up by experiments (Bergougnoux et al., 2014). In a similar manner, Bees et al. (1998b) identified how Stommel retention zones in circulatory flow (as a projection of Langmuir circulation) for positively buoyant particles could be eroded by an oscillatory shear perturbation, resulting in escape trajectories and resonance (see application of Melnikov's method in Hillary, 2003; Angilella, 2007). Swimming cells, particularly those that are gyrotactic (Kessler, 1985; O'Malley & Bees, 2012), have been observed to aggregate in turbulent flows, and mechanisms for this have been explored using model flow fields such as Taylor-Green flows (Durham et al., 2013). The importance of the interaction of shape and imposed shear in swimming cell dynamics has been reported in assorted studies (e.g. Torney & Neufeld, 2007; Durham et al., 2009; Zöttl & Stark, 2012, 2013; Bearon & Hazel, 2015; Hope et al., 2016). Here, we consider a model diatom in, progressively, Couette flow, Kolmogorov flow and cellular flow (a 2D analogue of Taylor-Green flow), and provide theoretical and numerical results for its Lagrangian dynamics. To our knowledge no other study explores the dynamics for non-inertial spheroidal particles in simple flows and elucidates the mechanisms in the manner herein described.

In summary, the primary aim of the paper is to demonstrate mechanisms for enhanced sedimentation of elongated plankton in the simplest possible flow fields and accumulation in particular parts of the flow. In section 2 we introduce a deterministic model to describe the trajectory of a negatively buoyant prolate spheroid. The particle's velocity is a sum of the fluid velocity and the settling velocity

of the particle, where the latter depends on particle orientation and aspect ratio. The rotation rate of the particle is determined by the shear, particle orientation and aspect ratio according to Jeffery's equation. In section 3 numerical simulations are performed in flows of increasing complexity. First we consider Couette flow, which has uniform shear rate, and thus particles undergo Jeffery orbits. We identify clear mechanisms for how shear modifies the sedimentation speed: in vertical shear, preferential flow alignment and aggregation in down-welling regions both increase sedimentation, whereas in horizontal shear the sedimentation is reduced due only to alignment. For Couette flow, the modification to sedimentation speed is independent of the magnitude of the shear and increases with aspect ratio. We then consider Kolmogorov flow, a simple uni-directional flow with non-constant shear. In vertical Kolmogorov flow elongated particles also have an enhanced sedimentation speed because of preferential flow alignment and aggregation in down-welling regions, an effect that increases with the magnitude of shear. In horizontal Kolmogorov flow we find there is aggregation in regions of high-shear where the sedimentation speed is minimum. The final flow field considered is two-dimensional cellular flow. We demonstrate how enhanced sedimentation due to aggregation in down-welling regions is still evident for this more complex flow. Furthermore, we find that spatially projected trajectories can intersect and give rise to chaotic dynamics, which is associated with a depletion of particles within so called retention zones. Finally, we provide some concluding remarks.

2. Model

Whilst diatoms, and microorganisms more generally, have a vast range of shapes, more complex morphologies share much of the dynamics of spheroids. For tractability and simplicity, we consider the deterministic motion of a prolate spheroid to represent a diatom chain, centred at position $\mathbf{x}$ with symmetry axis given by the unit vector $\mathbf{p}$. As reported in Ardekani et al. (2017), diatom size is small compared to the Kolmogorov length scale and the diatom to sea water density ratio typically is within the range 1 to 1.3. Furthermore, the particle rotational relaxation times are shorter than the translational relaxation time, which itself is at least a thousand times smaller than typical relaxation times of oceanic turbulent flows induced around the particles. Here, we shall only consider steady flows, and assume the particles are much smaller than flow length scales. Therefore, we follow the reasoning in Voth & Soldati (2017) and Ardekani et al. (2017) such that if the spheroid is advected at the local fluid velocity, $\mathbf{u}$, and sinks with settling velocity $\mathbf{v}_s$, which depends on particle orientation, then $\mathbf{x}$ is governed by

$$\frac{d\mathbf{x}}{dt} = \mathbf{u} + \mathbf{v}_s(\mathbf{p}). \tag{2.1}$$

Rotation of the particle is determined as a function of the vorticity $\boldsymbol{\omega}$ and rate of strain tensor $\mathbf{E}$ of the flow field as specified by Jeffery's equation,

$$\frac{d\mathbf{p}}{dt} = \frac{1}{2}\boldsymbol{\omega} \times \mathbf{p} + \beta(\mathbf{I} - \mathbf{pp}) \cdot \mathbf{E} \cdot \mathbf{p}, \tag{2.2}$$

where the shape factor β is given for a prolate spheroid as a function of the aspect ratio, $\mathscr{A}_R$, such that

$$\beta = \frac{\mathscr{A}_R^2 - 1}{\mathscr{A}_R^2 + 1}. \tag{2.3}$$

The settling velocity, $\mathbf{v}_s(\mathbf{p})$, can be expressed as

$$\mathbf{v}_s = v_s^{min}\mathbf{e}_g + (v_s^{max} - v_s^{min})(\mathbf{e}_g \cdot \mathbf{p})\mathbf{p}, \tag{2.4}$$

where the maximum sinking speed of v_s^{max} occurs when the symmetry axis, $\mathbf{p}$, is vertical and so aligned with the unit gravity vector $\mathbf{e}_g$, and the minimum sinking speed of v_s^{min} occurs when $\mathbf{p}$ is horizontal. We also introduce the parameter s_r which measures how the the ratio of sink speeds is enhanced above unity, the value for a sphere, defined as

$$s_r = \frac{v_s^{max}}{v_s^{min}} - 1. \tag{2.5}$$

The ratio of v_s^{max} to v_s^{min} is inversely proportional to the resistance functions, given by Kim & Karrila (2005) for a prolate spheroid, from which we can write s_r as a function of the aspect ratio, yielding

$$s_r = 2\frac{-2e+(1+e^2)L}{2e+(3e^2-1)L} - 1, \tag{2.6}$$

where

$$L = \ln\left(\frac{1+e}{1-e}\right), \tag{2.7}$$

and e is the eccentricity of the generating ellipse, given by

$$e = \sqrt{1-\frac{1}{\mathscr{A}_R^2}}. \tag{2.8}$$

The numerical values for the velocity ratio computed using these expressions agree with those used by Ardekani et al. (2017) for all values of $\mathscr{A}_R$ considered here. In the limit of $\mathscr{A}_R \to 1$, $s_r \to 0$, as expected for a sphere.

We consider fluid velocity and particle translation constrained to the $x-y$ plane, with $\mathbf{p} = (\sin\theta, \cos\theta)^T$ and $\omega = \omega\mathbf{k}$, where we take $\{\mathbf{i},\mathbf{j},\mathbf{k}\}$ as unit vectors in the direction of the x, y and z axes. We note that the unit gravity vector $\mathbf{e}_g = -\mathbf{j}$. Particle orientation is thus specified through the time-evolution of angle θ (e.g. see Bearon et al., 2011), such that

$$\dot{\theta} = -\frac{1}{2}\omega + \beta(\sin 2\theta E_{11} + \cos 2\theta E_{12}). \tag{2.9}$$

We non-dimensionalise all velocities based on v_s^{iso}, the average sink speed assuming an isotropic distribution of orientations, given by

$$v_s^{iso} = \frac{v_s^{max} + v_s^{min}}{2}. \tag{2.10}$$

Hence, the components of the non-dimensional settling velocity are

$$\mathbf{v}_s \cdot \mathbf{i} = -\frac{2s_r}{s_r+2}\sin\theta\cos\theta, \tag{2.11}$$

$$\mathbf{v}_s \cdot \mathbf{j} = -\frac{2}{s_r+2}(s_r\cos^2\theta + 1). \tag{2.12}$$

The full system of governing equations thus consists of the equation for particle position, (2.1), with components of the settling velocity given by equations (2.11,2.12), coupled to the equation for particle orientation, (2.9). In the following results section, a range of flow fields will be considered, and the effect of shape, as described by the aspect ratio, $\mathscr{A}_R$, will be examined. Note that the parameters β and s_r which appear in the governing equations are specified as functions of $\mathscr{A}_R$ in equations (2.3,2.6-2.8). The governing equations are solved using the ode15s solver in MATLAB R2016a.

3. Results

3.1 *Couette Flow*

We first consider Couette flow, which has the property of uniform shear so that the rotation rate only depends on particle orientation, and not particle position. The numerical simulations are typically run for the duration of one complete Jeffery orbit T, which in uniform shear, γ, is given by

$$T(\gamma, \mathscr{A}_R) = 4\pi/\gamma\sqrt{1-\beta^2}, \tag{3.1}$$

where we recall the shape parameter, β, is specified as a function of $\mathscr{A}_R$ in equation (2.3). Noting that velocity is non-dimensionalised on v_s^{iso}, in the absence of flow, for a uniform distribution of particle orientations the average downwards transport is expected to equal T. Hence, we can compare the downwards transport in the presence of flow with this expected value to investigate how shear and shape affect the downwards transport.

For uniform vertical shear, $\mathbf{u} = \gamma x\mathbf{j}$, we have vorticity $\omega = \gamma$ and strain $E_{11} = 0$, $E_{12} = \gamma/2$, so particle position and orientation are governed by

$$\dot{x} = -\frac{2s_r}{s_r+2}\sin\theta\cos\theta, \tag{3.2}$$

$$\dot{y} = \gamma x - \frac{2}{s_r+2}(s_r\cos^2\theta+1), \tag{3.3}$$

$$\dot{\theta} = \frac{\gamma}{2}(-1+\beta\cos 2\theta). \tag{3.4}$$

Numerical simulations were performed with particles initially at the origin, for a range of initial orientations, θ_0. In figure 1(a), we see that as a particle with initial orientation $\theta_0 = \pi/2$ begins to rotate anti-clockwise, it has a negative horizontal component of settling velocity. This results in the particle moving into down-welling flow. The particle continues to rotate, and we see it spends more time at the left-hand side of the trajectory (in more downwards flow) where it is vertically aligned. For the given parameters of $\gamma = 1$ and aspect ratio $\mathscr{A}_R = 20$, the duration of one complete Jeffery orbit is given by $T = 126$ and so we see a significantly enhanced downwards transport compared to the expected value in the absence of flow.

For a particle with initial orientation $\theta_0 = 0$, figure 1(b), as the particle begins to rotate anti-clockwise it has a positive horizontal component of settling velocity resulting in the particle moving into up-welling flow. However, we again see that the particle spends more time at the left-hand side of the trajectory (in more downwards flow) where it is vertically aligned.

By considering these example trajectories, we can identify two mechanisms for enhanced sedimentation. Firstly, particles preferentially align with the flow so that they spend more time settling at the maximum sinking speed. Secondly, particles spend more time in faster down-welling flow. These two effects can be identified if we compute the time-averaged downwards component of total velocity, i.e. sedimentation speed, given by

$$V_s = \frac{1}{T}\int_0^T -\gamma x + \frac{2}{s_r+2}(s_r\cos^2\theta+1)dt. \tag{3.5}$$

There are two contributions to the sedimentation speed: the first term is downwards advection by the flow, and for vertical shear flow, the average value of this is determined by the average horizontal

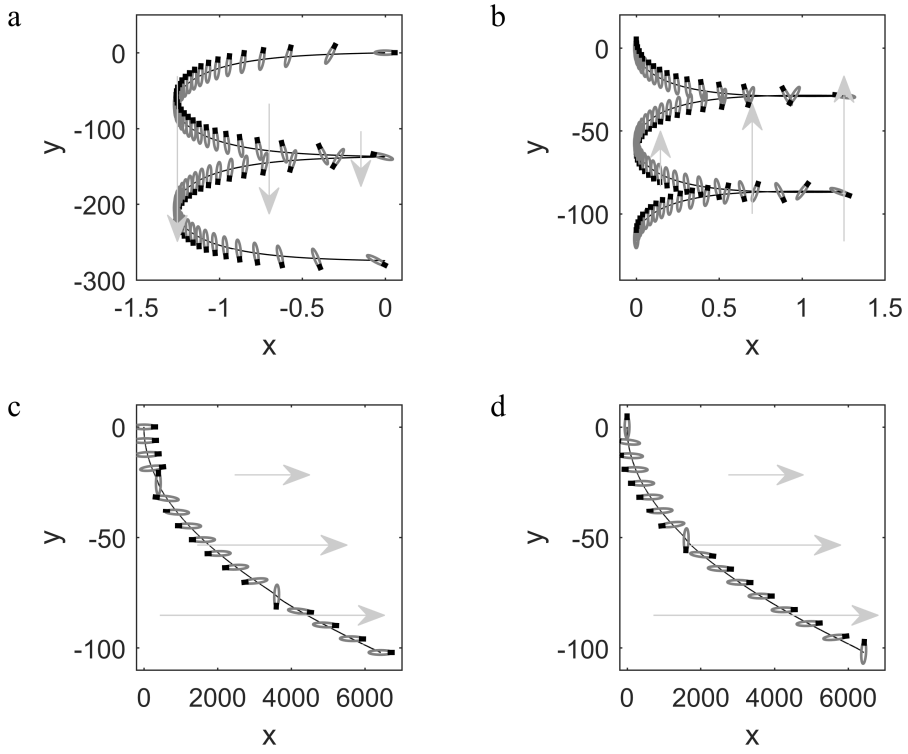

FIG. 1. Example trajectories of duration $T(1,20)$ for vertical (a,b) and horizontal (c,d) shear with shear rate $\gamma = 1$ and aspect ratio $\mathscr{A}_R = 20$. Particles are initially at the origin with orientation either $\theta_0 = \pi/2$ (a,c) or $\theta_0 = 0$ (b,d). Particles are plotted at uniform time increments with orientation $\theta = 0$ indicated by black dot.

position; the second term measures orientation-dependent particle settling and captures the non-uniform rotation rate of particles undergoing Jeffery orbits. For vertical shear flow, this latter contribution will lead to enhancement of the sedimentation speed because particles preferentially align with the flow. We denote the two contributions as V_s^{adv} and V_s^{sed}:

$$V_s^{adv} = \frac{1}{T}\int_0^T -\gamma x dt, \quad V_s^{sed} = \frac{1}{T}\int_0^T \frac{2}{s_r+2}(s_r\cos^2\theta+1)dt. \tag{3.6}$$

We shall now show that both these effects are independent of the magnitude of the shear.

First we compute the horizontal position as a function of orientation, making use of equations (3.2,3.4):

$$\begin{aligned}\frac{dx}{d\theta} = \frac{\dot{x}}{\dot{\theta}} &= \frac{2s_r}{\gamma(s_r+2)}\frac{\sin 2\theta}{(1-\beta\cos 2\theta)},\\ \Rightarrow \gamma x &= \frac{1}{\beta}\frac{s_r}{s_r+2}\ln\frac{1-\beta\cos 2\theta}{1-\beta\cos 2\theta_0,}\end{aligned} \tag{3.7}$$

where we take initial conditions that at $t=0$, $x=0, \theta=\theta_0$.

We can then compute V_s^{adv} and V_s^{sed} as a function of only the aspect ratio and initial particle orientation (details in appendix A), such that

$$V_s^{adv} = -\frac{\sqrt{1-\beta^2}}{2\pi\beta}\frac{s_r}{s_r+2}\int_0^{2\pi}\frac{1}{1-\beta\cos 2\theta}\ln\frac{1-\beta\cos 2\theta}{1-\beta\cos 2\theta_0}d\theta, \tag{3.8}$$

$$V_s^{sed} = 1+\frac{s_r}{\beta(s_r+2)}\left(1-\sqrt{1-\beta^2}\right). \tag{3.9}$$

If we suppose that the initial orientation is randomly sampled from $U(-\pi,\pi)$, the expected value of V_s^{adv} is given by

$$\overline{V_s^{adv}} = -\frac{\sqrt{1-\beta^2}}{4\pi^2\beta}\frac{s_r}{s_r+2}\int_0^{2\pi}\int_0^{2\pi}\frac{1}{1-\beta\cos 2\theta}\ln\frac{1-\beta\cos 2\theta}{1-\beta\cos 2\theta_0}d\theta d\theta_0. \tag{3.10}$$

The value of V_s^{sed} and expected sedimentation speed, $\overline{V_s} = \overline{V_s^{adv}} + V_s^{sed}$ are computed as an increasing function of the aspect ratio in figure 2. Also shown is the average sedimentation speed, that is the net vertical displacement divided by trajectory duration, T, of $N=100$ simulations with initial orientation randomly sampled from $U(-\pi,\pi)$, demonstrating good agreement with the analytic predictions. We note that whilst the expected sedimentation speed is independent of shear, this result only holds for particles undergoing complete Jeffery orbits. In particular, the case of zero shear, $\gamma=0$, is singular, as particles will not rotate and so the expected sedimentation speed will only depend on the initial orientation of cells. In simulations where the initial orientation is randomly sampled from $U(-\pi,\pi)$, the average sink speed will be unity (non-dimensionalised with v_{iso}).

Generalizing, any flow of the form $\mathbf{u} = \gamma g(x)\mathbf{j}$ with differentiable function $g(x)$, gives the coupled system

$$\dot{x} = -\sigma\sin 2\theta, \tag{3.11}$$

$$\dot{y} = \gamma g(x) - 2\sigma(\cos^2\theta + s_r^{-1}), \tag{3.12}$$

$$\dot{\theta} = -\frac{\gamma}{2}g'(x)(1-\beta\cos 2\theta), \tag{3.13}$$

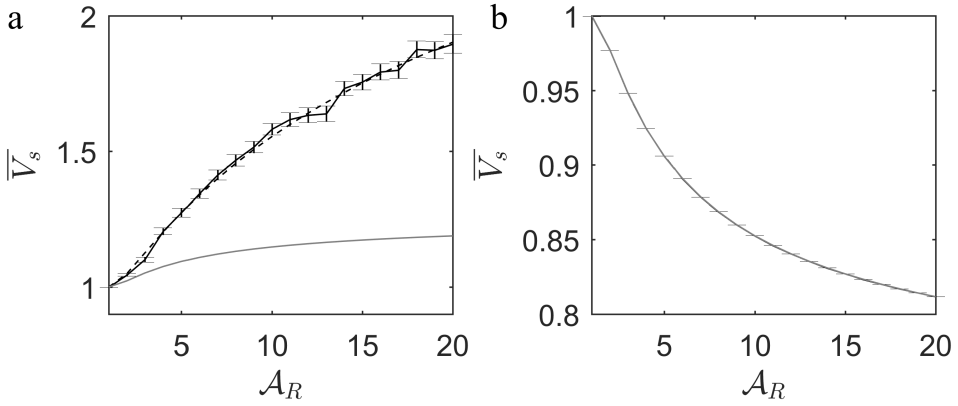

FIG. 2. Expected sedimentation speed, $\overline{V_s}$ as a function of aspect ratio, $\mathscr{A}_R$. Dash line is analytic expression for sedimentation speed, $\overline{V_s} = \overline{V_s^{adv}} + V_s^{sed}$, lower grey line is direct settling contribution, V_s^{sed}. Note the analytic expression is independent of shear rate, γ. Solid line is average value from numerical simulations of $N = 100$ trajectories of duration $T(1, \mathscr{A}_R)$ with $\gamma = 1$ and particles initially located at the origin with random initial orientation. Error bars indicate standard error. (a) Vertical shear. (b) Horizontal shear, for which $V_s^{adv} = 0$.

where $\sigma = s_r/(s_r+2)$. Once solutions $\theta(t)$ and $x(t)$ of equations 3.11 and 3.13 are known we may compute

$$y(t) = y(0) + \int_0^t \gamma g(x(t')) - 2\sigma(\cos^2\theta(t') + s_r^{-1})\, dt', \tag{3.14}$$

or, alternatively, changing variables to y via substitution of 3.12 and keeping track of orbits. By writing $dx/d\theta = \dot{x}/\dot{\theta}$ and integrating, we find the constant of motion

$$K = \frac{\sigma}{2\beta} e^{-\Gamma g(x)} \left(-1 + \beta\cos 2\theta\right), \tag{3.15}$$

where $\Gamma = \beta\gamma/\sigma$. The expression for $K(x,\theta)$ allows us to plot trajectories in the $x-\theta$ phase space, and write

$$\dot{x} = e^{\Gamma g(x)} K_\theta \quad \text{and} \quad \dot{\theta} = -e^{\Gamma g(x)} K_x, \tag{3.16}$$

which we may transform to standard Hamiltonian structure via the identification

$$H(q,p) = K(\theta, x), \tag{3.17}$$

with

$$q = \theta, \quad p = \int \frac{1}{\mu(x)} dx, \quad \text{where} \quad \mu(x) = e^{\Gamma g(x)}. \tag{3.18}$$

This yields the system

$$\dot{p} = H_q \quad \text{and} \quad \dot{q} = -H_p \tag{3.19}$$

(see Hojman, 2015).

In the Couette flow case above $g(x) = x$ and thus $q = \theta$ and $p = -e^{-\Gamma x}/\Gamma$, with Hamiltonian $H(q,p) = -\frac{\gamma}{2} p\,(-1 + \beta\cos 2q)$.

For uniform horizontal shear we expect to see a reduction in sedimentation speed. Firstly, because particles preferentially align with the flow, they will spend more time settling at the *minimum* sinking speed and thus there should be a reduction in V_s^{sed} with increasing aspect ratio. This is depicted in figure 1(c,d) and figure 2(b). Secondly, because the vertical component of the flow is zero, there is no enhancement of sedimentation due to preferential location in certain regions of the flow, hence $V_s^{adv} = 0$. In particular, for flow field $\mathbf{u} = -\gamma y \mathbf{i}$, we have vorticity and strain $\omega = \gamma, E_{11} = 0, E_{12} = -\gamma/2$, so the governing equations are given by

$$\dot{x} = -\gamma y - \frac{2s_r}{s_r+2}\sin\theta\cos\theta, \tag{3.20}$$

$$\dot{y} = -\frac{2}{s_r+2}(s_r\cos^2\theta+1), \tag{3.21}$$

$$\dot{\theta} = \frac{\gamma}{2}(-1-\beta\cos 2\theta). \tag{3.22}$$

The sedimentation speed, V_s, now only has a settling component which is given by

$$V_s = V_s^{sed} = \frac{1}{T}\int_0^T -\frac{2}{s_r+2}(s_r\cos^2\theta+1)dt = 1 - \frac{s_r}{\beta(s_r+2)}\left(1-\sqrt{1-\beta^2}\right). \tag{3.23}$$

In figure 2(b) we see good agreement with this analytic expression and the average of $N = 100$ simulations with initial orientation sampled uniformly from $[0, 2\pi]$.

To summarize, in vertical shear there are two contributions which enhance the sedimentation speed: preferential alignment with the flow and preferential aggregation in down-welling regions. In horizontal shear there is only a reduction in sedimentation speed due to preferential alignment with the flow.

3.2 *Kolmogorov Flow*

We next consider Kolmogorov flow, an example unidirectional flow with non-constant shear. We choose to non-dimensionalise based on the lengthscale of variation in the flow, so that for vertical flow, the velocity is given by

$$\mathbf{u} = \gamma\sin x\mathbf{j}, \tag{3.24}$$

which gives the same governing equations as for uniform vertical shear but with the shear rate now a function of horizontal position and given by $\gamma\cos x$, such that

$$\dot{x} = -\frac{2s_r}{s_r+2}\sin\theta\cos\theta, \tag{3.25}$$

$$\dot{y} = \gamma\sin x - \frac{2}{s_r+2}(s_r\cos^2\theta+1), \tag{3.26}$$

$$\dot{\theta} = \frac{\gamma\cos x}{2}(-1+\beta\cos 2\theta). \tag{3.27}$$

Equation 3.15 in section 3.1 with $g(x) = \sin(x)$ yields the constant of motion

$$K = \frac{\sigma}{2\beta}e^{-\Gamma\sin(x)}\left(-1+\beta\cos 2\theta\right), \tag{3.28}$$

where $\Gamma = \beta\gamma/\sigma$, from which we can plot trajectories in the $x-\theta$ phase space (and compute the Hamiltonian system if desired).

Numerical simulations were performed with particles for a range of initial orientations, θ_0 and initial horizontal positions, x_0 as depicted in figures 3(a-d). In figure 3(a), we see that as a particle starting at the origin with initial orientation $\theta_0 = \pi/2$ begins to rotate anti-clockwise, it has a negative horizontal component of settling velocity. As the particle passes $x = -\pi/2$, where the downwards flow velocity is maximum and the shear is zero, the particle switches to clockwise rotation. The particle continues to move with a negative horizontal component of settling velocity until it is horizontal, $\theta = \pi/2$, at which point it reverses its horizontal trajectory. As for uniform vertical shear, the particle spends more time vertically aligned with the flow, and more time in faster moving downwards flow, which, for this example, is at the horizontal midpoint of the trajectory. In contrast, a particle initially orientated vertically at $x = 0.5$, figure 3(b), begins to rotate anti-clockwise and so has a positive horizontal component of settling velocity. As the particle passes $x = \pi/2$, the particle switches to clockwise rotation. The particle continues to move with a positive horizontal component of settling velocity until it is vertical, $\theta = 0$, at which point it reverses its horizontal trajectory. Again we see that the particle spends more time vertically aligned with the flow, and more time in more downwards flow, which, for this example, is at the horizontal end points of the trajectory. By inspecting the $x-\theta$ phase space of the dynamics, figure 3(e), we can identify a range of behaviours that depend on the choice of initial condition.

The results in this section are of a similar nature to those of the Hamiltonian dynamics documented in Zöttl & Stark (2012, 2013) for a spheroidal swimmer subject to Poiseuille flow. In their system in a channel or tube of non-dimensional radius 1, the flow may also be described by equations 3.11 to 3.13 with $g(x) = \bar{v}_f(r-1)^2$, where $\bar{v}_f$ is the ratio of maximum flow to swimming velocities. As both models describe spheroids, the viscous torques and thus orientational dynamics are identical. However, the particles presented here settle in a bipolar fashion, are not bounded horizontally by vertical channel walls and do not swim, so the dynamics for x and y differ accordingly. Nonetheless, Zöttl & Stark (2012, 2013) found constants of the motion for swimming spheroids in Poiseuille flow; in a similar manner, a three-dimensional extension is possible here for the current sedimentation system, yielding two constants of motion. The phase space for the Zöttl & Stark (2012) system revealed two types of trajectory: described as "swinging" and "tumbling" behaviour. A similar categorisation of trajectories in the phase space in figures 3 and 4 is possible for our system: there are three distinct types of trajectory, as follows.

1. A "*swinging*" motion about a fixed (negative) value of x, with closed orbits in the bottom-left of figure 3(e), as observed in figures 3(a) and 3(c).

2. A different variety of the above, a "*swaying*" motion in the closed orbit to the right of figure 3(e), as in figure 3(b). Particles can undergo substantial horizontal periodic motion with only a small oscillation in orientation.

3. A "*tumbling*" motion about $x = 0$ as represented by the trajectory in $x-\theta$ phase space in figure 3(e) with a monotone decrease in θ, for which, as can be observed in figure 3(d), the particle completely rotates.

In figure 4 we investigate the effect of shear strength. In figure 4(a) a particle initially horizontal at the origin undergoes complete Jeffery orbits and the enhanced sedimentation is similar to that found in uniform vertical shear. In contrast, for weaker shear, figure 4(b), with the same initial conditions, particles undergo less rotation over each horizontal periodic motion, and so the enhancement is reduced.

This can be further examined by considering the phase portraits in figures 4(c,d). We see that the region where particles undergo complete orientation orbits is larger for the higher shear case.

On computing the spatial position of $N = 1000$ particles initially at $y = 0$ with x_0 and θ_0 randomly sampled from $U(-\pi, \pi)$, from figure 5(a) we see that particles spend more time in the regions of maximum down-welling, close to $x = -\pi/2$, and less time in the up-welling regions, close to $x = \pi/2$, which results in an enhancement in sedimentation speed. As for the uniform vertical shear, we also expect an enhancement of sedimentation due to non-uniform rotation and hence particles spend more time vertically aligned with the flow. In figure 5(b) we see how the average sedimentation speed depends on aspect ratio and shear. In uniform vertical shear sedimentation was independent of the magnitude of the shear; for Kolmogorov flow the sedimentation speed is shear dependent and increases with the shear strength. To understand where this dependence on shear strength arises, we can consider equations (3.6,3.7) describing the sedimentation speed. We note that the result that the integrand of V_s^{adv} is independent of γ holds for any flow of the form $\mathbf{u} = \gamma g(x)\mathbf{j}$. However, whereas for uniform shear, on changing variables in the integral, the upper limit of integration with respect to θ was given by $\theta(T) = \theta_0$ for the time period T of a Jeffery orbit in shear rate γ, in the current case of non-uniform shear, the value of $\theta(T)$ will depend on the initial position and the shear. As the shear increases, the region of phase-space where complete orientation orbits (tumbling) occur increases; as is evident on comparing figure 4(c) and (d). Furthermore, as the shear increases, particles undergo less horizontal motion, and thus effectively experience approximately uniform shear. Therefore, we predict that the enhancement found in uniform shear will be an upper-bound on the enhancement that is possible for Kolmogorov flow. As is clear from figure 5(b), by increasing the shear from $\gamma = 1$ to $\gamma = 5$, we approach the uniform flow limit. However as the shear increases it is necessary to simulate a larger number of cells to get an accurate measure of the mean, because cells sample a much reduced horizontal range.

For horizontal Kolmogorov flow, the velocity is given by

$$\mathbf{u} = \gamma \sin y \mathbf{i}, \tag{3.29}$$

which gives the same governing equations as for uniform horizontal shear but with the shear rate now a function of vertical position and given by $\gamma \cos y$.

Numerical simulations were performed with particles for a range of values of shear, γ, aspect ratio, $\mathscr{A}_R$ and initial conditions, to illustrate the range of possible behaviours, figure 6(a-f). For $\gamma = 1, \mathscr{A}_R = 20$ we see a particle initially aligned vertically undergoes swinging motions as it sediments through the fluid. In contrast, a particle horizontally aligned remains horizontal and undergoes swaying motions as it descends through regions with varying shear. This maintenance of horizontal orientation is because, at this large value of $\mathscr{A}_R$, particles align strongly in the direction of the flow. This maintenance of horizontal orientation, $\theta = \pi/2$, is reinforced on considering the $\theta - y$ phase space, figure 6(g,h). A similar pattern is observed at stronger shear, $\gamma = 5$, and we observe that for particles initially vertical, translation is closely aligned with particle orientation. By reducing the aspect ratio to $\mathscr{A}_R = 5$, we see that particles initially orientated horizontally are rotated by the flow, 6(f).

As for uniform horizontal shear, horizontal Kolmogorov flow causes a reduction in the sedimentation speed (figure 7(b)). Also, in a similar manner to the vertical Kolmogorov flow case, the reduction in sedimentation found for horizontal uniform shear provides an upper-bound on the reduction that is possible for horizontal Kolmogorov flow. Furthermore, as the shear is not uniform, as particles sink through the layers the sedimentation speed varies with depth. This leads to trapping in high-shear horizontal layers, as previously observed for elongated swimming cells, albeit by a somewhat different mechanism (Bearon & Hazel, 2015; Rusconi et al., 2014).

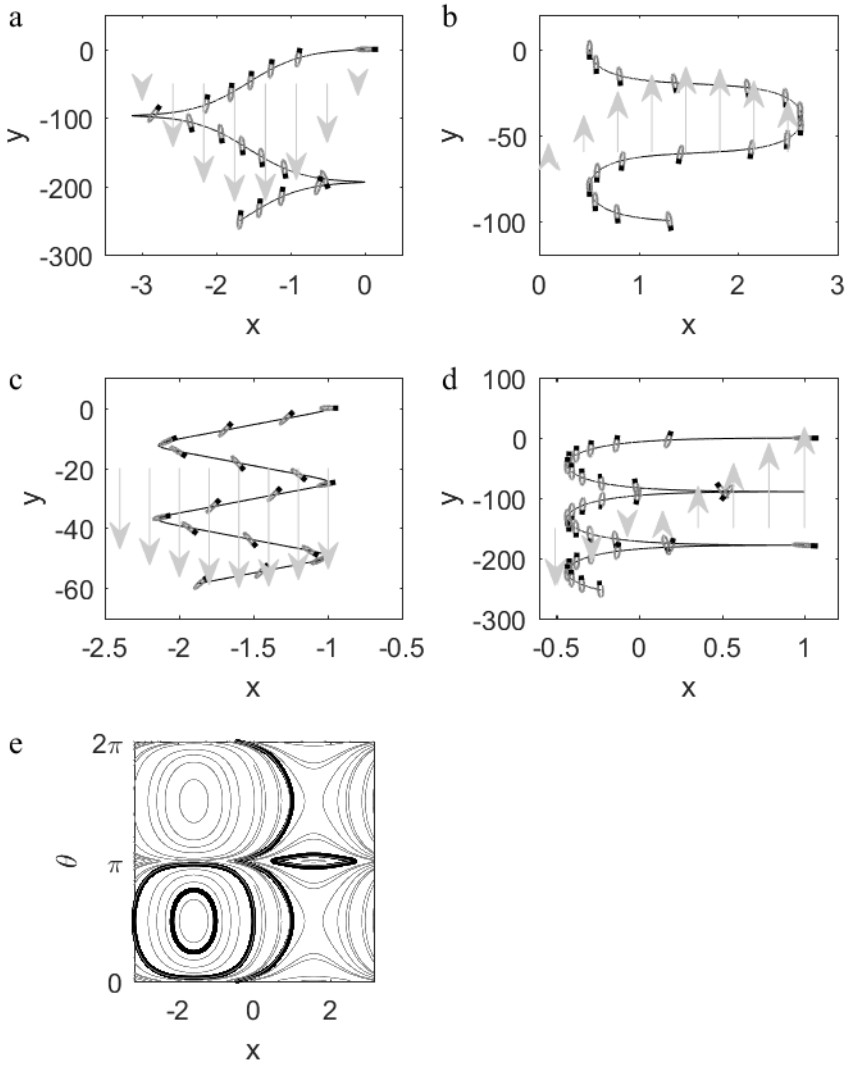

FIG. 3. Vertical Kolmogorov flow. (a-d) Example trajectories with aspect ratio $\mathscr{A}_R = 20$ and shear rate $\gamma = 1$. Initial conditions and duration: (a) $\theta_0 = \pi/2, x_0 = 0, T(1,20)$, (b) $\theta_0 = \pi, x_0 = 0.5, 1.5T(1,20)$, (c) $\theta_0 = \pi/2, x_0 = -1, 0.25T(1,20)$, (d) $\theta_0 = \pi/2, x_0 = 1, 1.5T(1,20)$. (e) Phase portrait of $x-\theta$ space, with trajectories depicted in (a-d) indicated in bold.

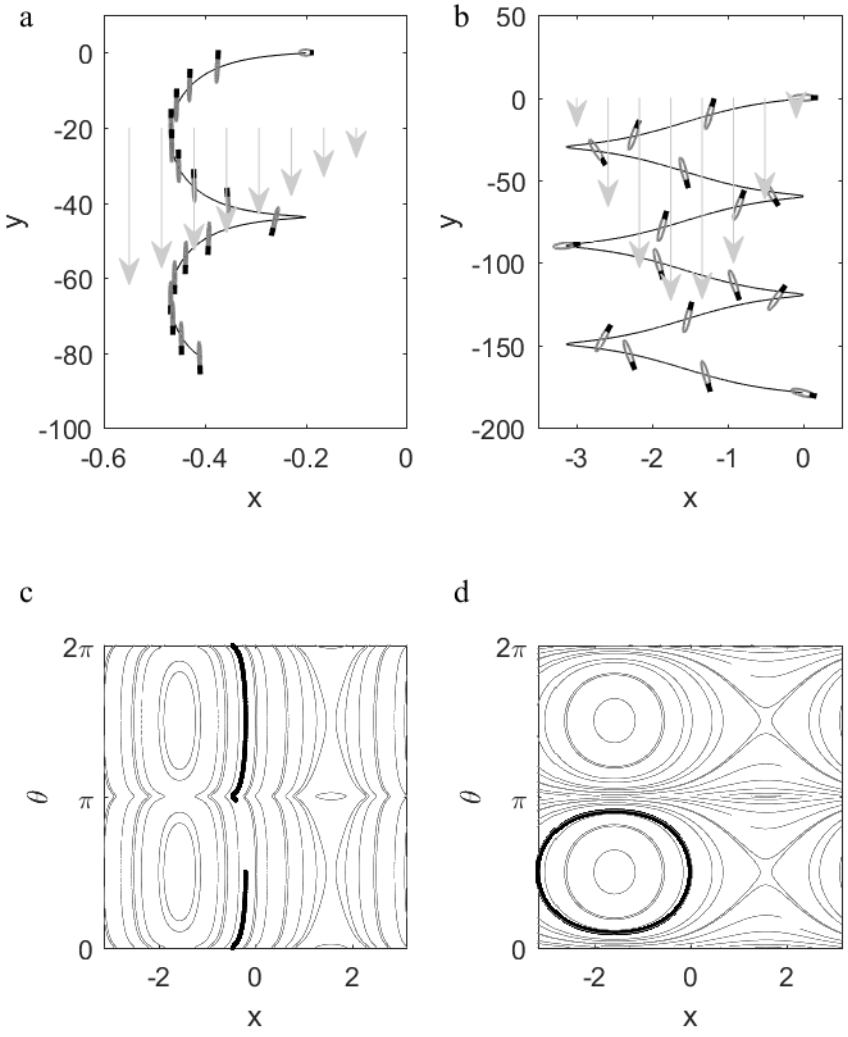

FIG. 4. Kolmogorov flow. (a,b) Example trajectories with aspect ratio $\mathscr{A}_R = 20$. (a) High shear rate $\gamma = 5$, initial condition $\theta_0 = \pi/2, x_0 = -0.1$ and duration $T(5,20)$. (b) Low shear rate $\gamma = 0.5$, initial condition $\theta_0 = \pi/2, x_0 = 0$ and duration $0.5T(0.5,20)$. Phase portrait of $x-\theta$ space, for (c) high shear rate, $\gamma = 5$, and (d) low shear rate, $\gamma = 0.5$, with trajectories depicted in (a,b) indicated in bold.

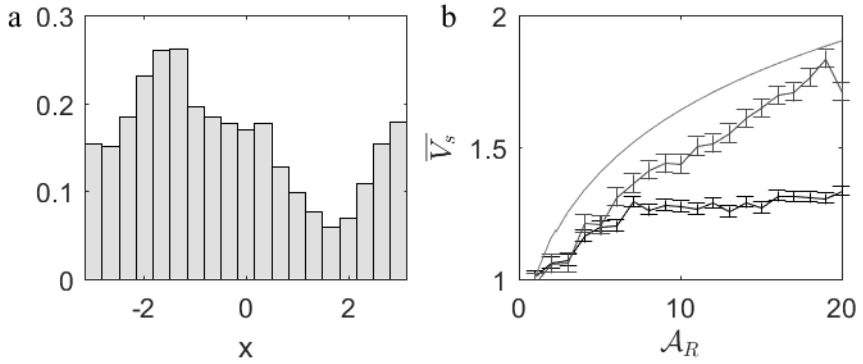

FIG. 5. Vertical Kolmogorov flow. (a) Histogram of horizontal position over a trajectory for $N = 1000$ particles with $\gamma = 20$, aspect ratio $\mathscr{A}_R = 20$, duration $T = 10$ initially at $y = 0$ with θ_0 and x_0 randomly sampled from $U(-\pi,\pi)$. The histogram is normalized as a probability density function. (b) Average sedimentation speed, $\overline{V_s}$, as a function of aspect ratio, $\mathscr{A}_R$ computed from trajectories of duration $T = 10$ initially at $y = 0$ with θ_0 and x_0 randomly sampled from $U(-\pi,\pi)$. Shear rate $\gamma = 1$ (black), $\gamma = 5$ (dark grey). Error bars indicate standard error. Simulations were performed for $N = 1000$ particles for $\gamma = 1$, $N = 10000$ for $\gamma = 5$. The expected sedimentation speed for vertical Couette flow, see figure 2, is re-plotted (light grey line) as the expected upper bound in the limit of large shear.

3.3 *Cellular Flow*

We now consider a simple two-dimensional flow field with spatially varying vorticity and strain. This can be viewed as an extension of the Kolmogorov flow field to allow for regions of both horizontal and vertical shear flow, and is specified as

$$\mathbf{u} = \gamma(-\cos x \sin y, \sin x \cos y), \tag{3.30}$$

with vorticity $\omega = 2\gamma \cos x \cos y$, and strain $E_{11} = \gamma \sin x \sin y$, $E_{12} = 0$. The governing equations are thus given explicitly as

$$\dot{x} = -\gamma \cos x \sin y - \frac{2s_r}{s_r+2} \sin\theta \cos\theta, \tag{3.31}$$

$$\dot{y} = \gamma \sin x \cos y - \frac{2}{s_r+2}(s_r \cos^2\theta + 1), \tag{3.32}$$

$$\dot{\theta} = -\gamma \cos x \cos y + \gamma\beta \sin 2\theta \sin x \sin y. \tag{3.33}$$

This system is equivalent to the cellular flow investigated in Shin & Maxey (1997). For spherical particles the system reduces to that of Mallier & Maxey (1991) or Bees et al. (1998b) and a Hamiltonian structure is easily found (and can be written in terms of action angle variables). For the (volume preserving perturbation) case where variation in settling velocities for a slightly spheroidal particle are taken into account but the particle elongation does not change the torque, Shin & Maxey (1997) showed that the possibility of permanent suspension by the flow persists (still yielding a coherent Stommel retention zone). For the more general case that includes a torque due to the rate-of-strain, they employ Poincaré

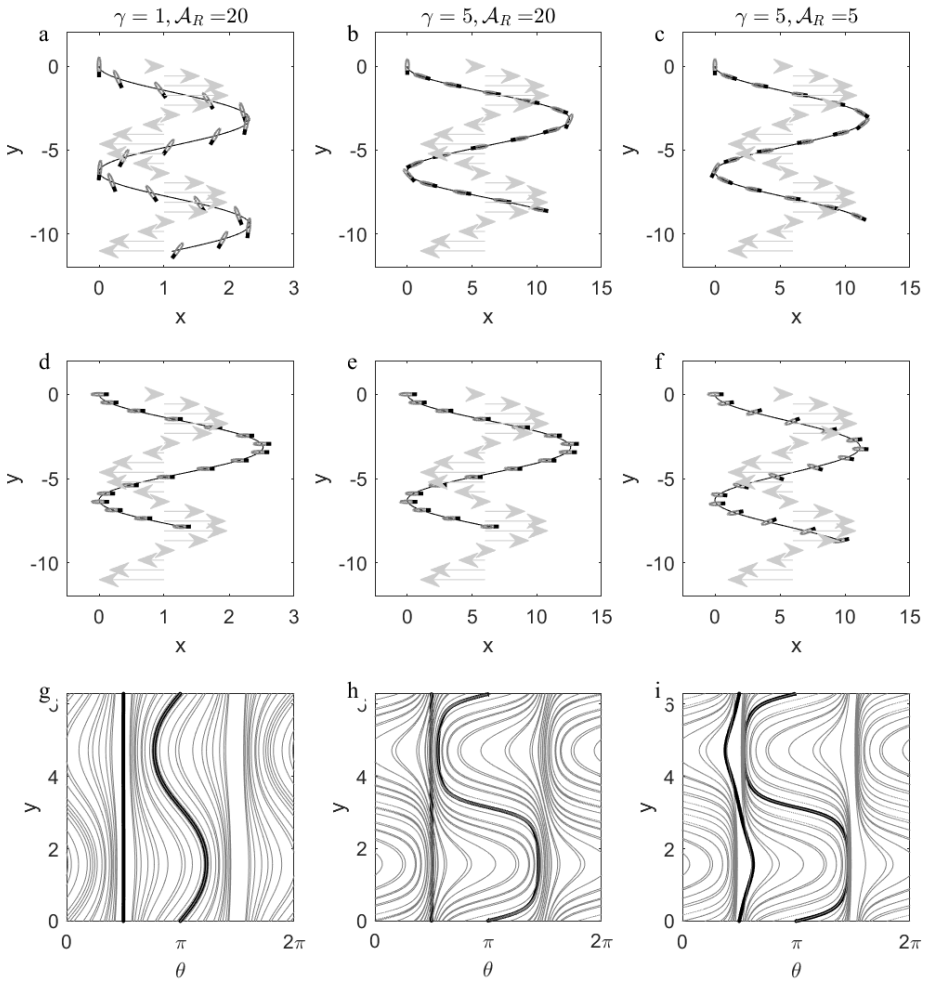

FIG. 6. Trajectories of particles of duration $T = 10$ initially at position $(x_0, y_0) = (0,0)$ in horizontal Kolmogorov flow for parameters $\gamma = 1, \mathscr{A}_R = 20$ (a,d,g); $\gamma = 5, \mathscr{A}_R = 20$ (b,e,h); and $\gamma = 5, \mathscr{A}_R = 5$ (c,f,h). Upper panels depict particles with initial orientation $\theta_0 = \pi$, and middle panels have $\theta_0 = \pi/2$. (g,h,i) Phase portrait of $\theta - y$ space, with trajectories depicted in (a-f) indicated in bold.

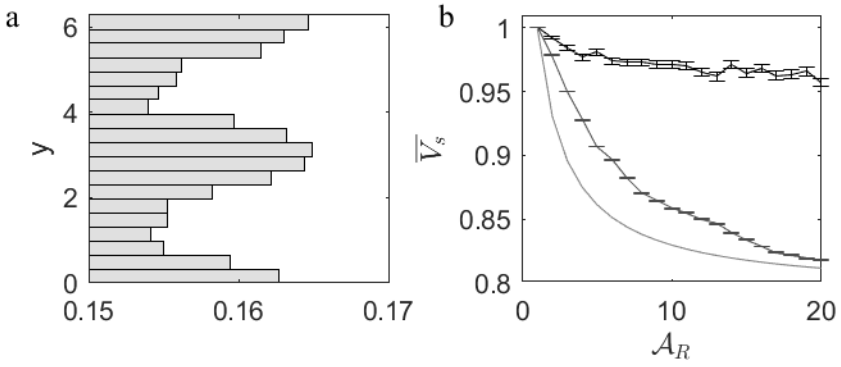

FIG. 7. Horizontal Kolmogorov flow. (a) Histogram of vertical position, modulo 2π, over a trajectory for $N = 1000$ particles with $\gamma = 1$, aspect ratio $\mathscr{A}_R = 20$, duration $T = 10$ initially at $x = 0$ with θ_0 and y_0 randomly sampled from $U(0, 2\pi)$. The histogram is normalized as a probability density function. (b) Average sedimentation speed, $\overline{V_s}$, as a function of aspect ratio, $\mathscr{A}_R$ computed from $N = 1000$ particles trajectories of duration $T = 10$ initially at $x = 0$ with θ_0 and y_0 randomly sampled from $U(0, 2\pi)$. Shear rate $\gamma = 1$ (black), $\gamma = 20$ (dark grey). Error bars indicate standard error. The expected sedimentation speed for horizontal Couette flow, see figure 2, is re-plotted (light grey line) as the expected lower bound in the limit of large shear.

sections to demonstrate numerically that the motion is chaotic. For buoyant particles in this cellular flow with an additional time-periodic shear perturbation, Bees et al. (1998b) explored Stommel retention zone escape trajectories and the emergence of separate resonant retention zones. Melnikov theory can be applied for the case of weak time-periodic perturbations (Hillary, 2003), including dissipative inertial terms in the particle motion (Angilella, 2007), to predict whether Stommel retention zones persist and horizontal dispersion dynamics. Here, we focus on enhanced setting rates in the cellular flow.

In figure 8, example trajectories and streamlines are shown. In the numerical simulations, particles of aspect ratio $\mathscr{A}_R = 20$ are simulated with various initial conditions. For comparison, also plotted is the corresponding trajectory for a sphere that simply sinks vertically downwards at unit speed and is advected by the flow. Note that we have non-dimensionalised velocities based on the average sink speed of a particle of aspect ratio $\mathscr{A}_R = 20$ assuming an isotropic distribution of orientations, so the comparison with the sinking sphere enables the effects of anisotropic drag and non-uniform rotation to be examined. In figure 8(b), we see that for $\gamma = 1$, particles with the same initial position $(x_0, y_0) = (\pi, 0)$ but with either vertical ($\theta_0 = 0$) or horizontal ($\theta_0 = \pi/2$) initial orientation have divergent trajectories. The sedimentation speed is less than the sphere for the initially vertical particle but greater for the initially horizontal particle. At higher shear rates, cells can undergo more complex trajectories. In 8(c), particles are initially located at $(x_0, y_0) = (5\pi/4, -\pi)$; and we again see a difference in sedimentation speed dependent on the initial orientation.

To investigate systematically the impact of shear and shape, we computed the trajectories of $N = 1000$ particles with initial (x, y, θ) sampled from $U(0, 2\pi)$. In figure 8, 100 example trajectories for sample $\mathscr{A}_R$ and γ are shown. For spheres, for $\gamma > 1$, particles are trapped in Stommel retention zones. For spheres sinking at unit speed, the total particle velocity is given by $\dot{\mathbf{x}} = \mathbf{u} - \mathbf{j}$ which has streamfunction

$$\psi = \gamma \cos(x)\cos(y) + x,$$

defined in the standard way: $\dot{x} = \frac{\partial \psi}{\partial y}, \dot{y} = -\frac{\partial \psi}{\partial x}$. The streamline for the retention zone can be identified by obtaining the value of the streamfunction where the total particle velocity is zero. Easily identifiable points are located at $x_s = \pi/2, \gamma \cos y_s = 1$, yielding the streamline $\psi_s = \pi/2$ and at

$x_s = 3\pi/2, \gamma \cos y_s = -1$, yielding the streamline $\psi_s = 3\pi/2$. The latter streamline is depicted as a thick red line in figure 9. As the aspect ratio is increased, we see the trajectories become more complex (for example, trajectories projected onto the $x-y$ plane can intersect). This is due to the settling velocity being dependent on orientation for non-spherical particles, and thus two particles at the same position with different orientations can sink in different directions. Furthermore, on comparing the effect of shape at strong shear ($\gamma = 1.5$) we see that only a small fraction (13% for $\mathscr{A}_R = 20$, and 1% for $\mathscr{A}_R = 20$) of particles are retained in the retention zone for a duration $T_R = 100$. Furthermore, particles not retained are ejected at significantly earlier times ($T_R < 40$) suggesting that a retention zone is still present for the non-spherical particles, but that the retention zone, defined in the three-dimensional (x, y, θ) space, reduces as the aspect ratio of particles increases.

Further investigation of the effect of shear and aspect ratio on the distribution of particles is presented in the histograms for the spatial distribution, figure 10, where we see that increasing both the shear rate and aspect ratio results in accumulation of particles in regions of down-welling flow. As a consequence of this preferential aggregation in down-welling regions, we see in figure 11(a) that the sedimentation speed increases with aspect ratio and also with shear strength, as found for vertical Kolmogorov flow. Finally, to support the claim that non-spherical particles exhibit chaotic motion, we compute the long-time Lyapunov exponents for two sample initial conditions, see figure 11(b).

4. Conclusion

Our aim in this paper was to explore the dynamics of sedimenting spheroids in the simplest possible flows, providing some clarity for the mechanisms involved in recent experiments (Ruiz et al., 2004) and numerical simulations (Ardekani et al., 2017) of settling diatoms in isotropic turbulence. We have built up the mechanistic description from Couette flow (constant shear rate) through Kolmogorov flow (unidirectional flow with non-constant shear) to cellular flow.

The Couette flow case can be split into two parts, vertical and horizontal shear flows. For vertical shear we find that the flow induces enhanced sedimentation dynamics through precisely two mechanisms: preferential alignment of the spheroidal particles with the flow and their aggregation in down-welling regions due to the orientation dependent horizontal and vertical components of their settling velocity. We demonstrated that these effects are independent of the magnitude of the non-zero shear, and that the dynamics for non-spherical particles possess Hamiltonian structure. However, for horizontal shear flow there is only one mechanism due to the particles aligning with the flow, which causes a reduction in the sedimentation speed. For Kolmogorov flow similar mechanisms are at work as for shear flow, except that translation in the flow field gives rise to variations in the rotation of the particles. Again we find a Hamiltonian structure for the sedimentation of non-spherical particles in vertical shear, with three types of trajectory in phase space: "tumbling," "swinging" and "swaying" trajectories. The first two of these have been observed in the dynamics for the swimming of spheroidal cells in Poiseuille flow (Zöttl & Stark, 2012, 2013). Elongated particles spend more time in down-welling regions of the flow with vertically aligned orientation, and thus have an enhanced sedimentation speed over spherical particles. Unlike the constant shear case, the enhancement to sedimentation is dependent on the magnitude of shear, with an enhancement ratio of 1.7 for a particle aspect ratio of 20 and a non-dimensional shear rate of 1. The frequency of tumbling depends on the aspect ratio and shear. Of particular rel-

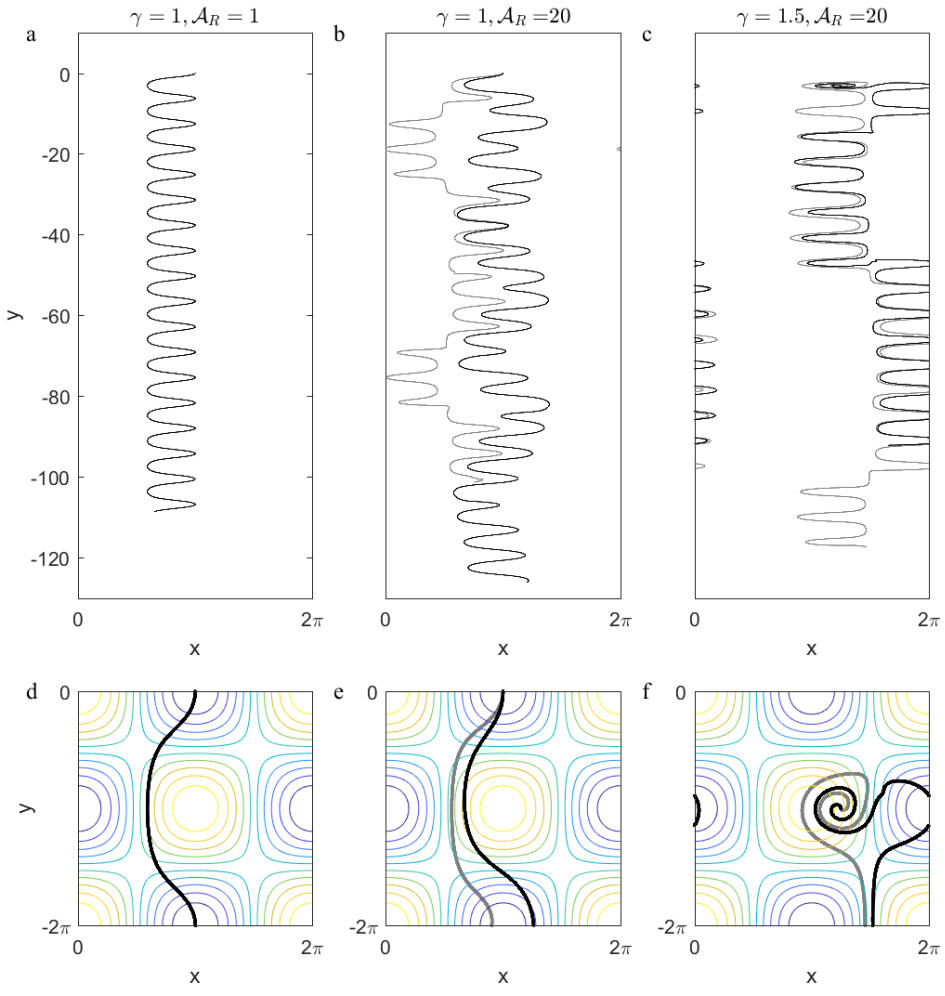

FIG. 8. Trajectories of particles of duration $T = 100$ in cellular flow with shear rate, $\gamma = 1$ and $\gamma = 1.5$ for aspect ratio $\mathscr{A}_R = 1$ (sphere), and $\mathscr{A}_R = 20$. The horizontal component x is displayed modulo 2π. Initial position $(x_0, y_0) = (\pi, 0)$ in (a,b), $(x_0, y_0) = (5\pi/4, -\pi)$ in (c) with initial orientation $\theta_0 = 0$ (grey line), $\theta_0 = \pi/2$ (black line). Lower panels show initial sections of the trajectories overlaid on streamlines of the flow. The colour coding is such that yellow represents anticlockwise rotation (negative vorticity) and blue clockwise rotation (positive vorticity)

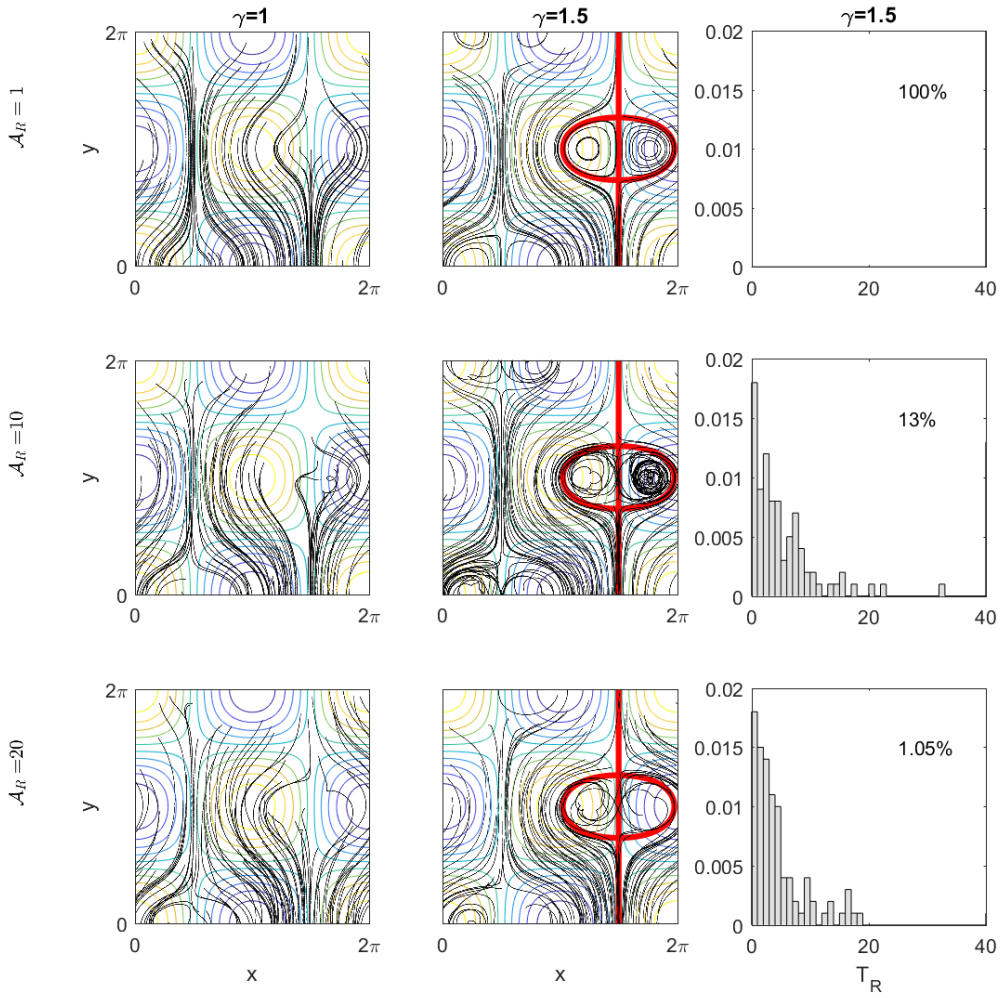

FIG. 9. Trajectories of particles of duration $T = 100$ in cellular flow with shear rate $\gamma = 1$ and $\gamma = 1.5$ for aspect ratio $\mathscr{A}_R = 1$ (sphere), and $\mathscr{A}_R = 10, 20$. Numerical simulations performed with $N = 1000$ particles with x_0, y_0 and θ_0 randomly sampled from $U(0, 2\pi)$. To aid visualisation, the vertical axes are restricted to $y \in [0, 2\pi]$, and the horizontal component x is displayed modulo 2π. In the left-hand two columns, 100 trajectories are plotted (black lines), and streamlines of the flow plotted as in figure 8. The thick red-lines indicate the retention zone, $\gamma\cos(x)\cos(y) + x = 3\pi/2$, for spherical particles. The right-hand normalised histograms are time spent, T_R, in the retention zone of particles initially located in the retention zone, with the number remaining in the retention zone for the entire duration $T = 100$ of the simulation indicated as a percentage.

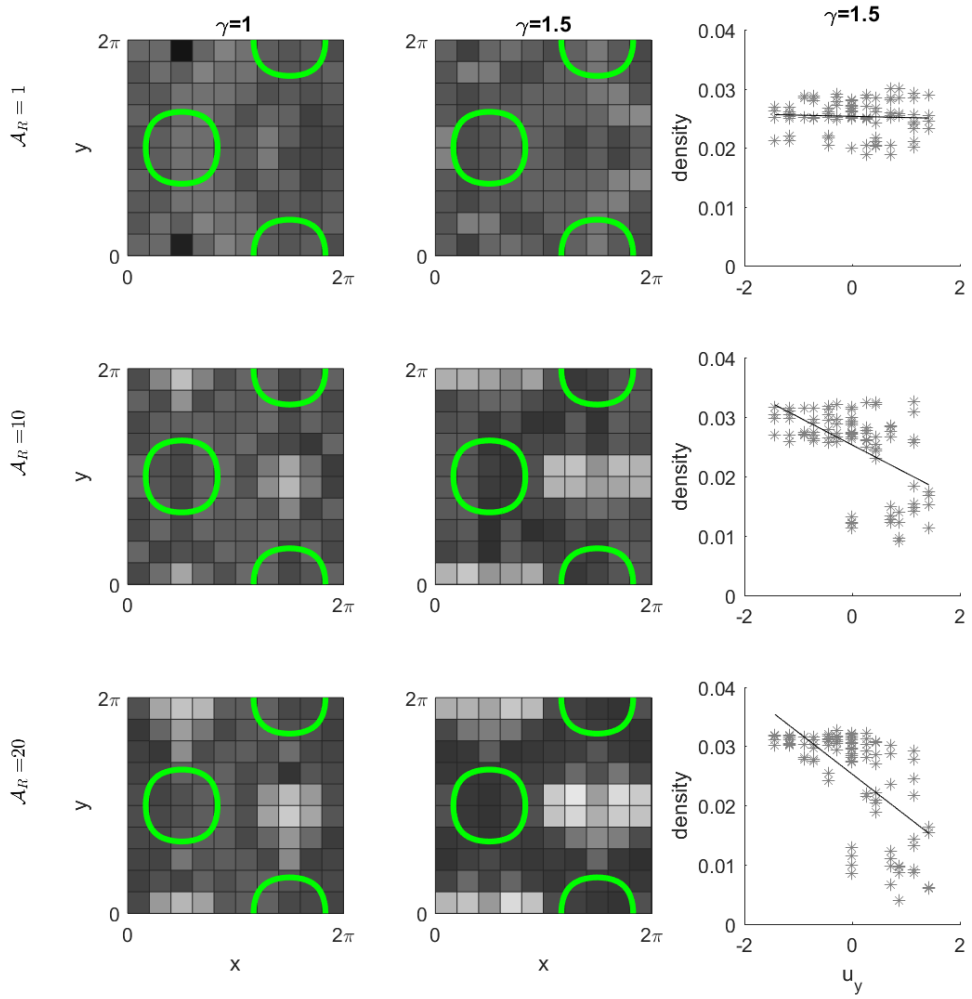

FIG. 10. Histograms of the distribution of spatial position modulo 2π for particle paths in cellular flow with shear rate, $\gamma = 1$ and $\gamma = 1.5$ of duration $T = 100$ for aspect ratio $\mathscr{A}_R = 1$ (sphere), and $\mathscr{A}_R = 10, 20$. Numerical simulations performed with $N = 1000$ particles with x_0, y_0 and θ_0 randomly sampled from $U(0, 2\pi)$. The greyscale represents a linear gradient from a normalised concentration of 0 (white) to 1.6 (black). Thick green lines overlaid on the histogram indicate $u_y = -\gamma/2$ and are to aid visualisation of the down-flow regions. The right-hand column shows the correlation between down-flow regions and particle aggregation; the black line is a linear regression on the data points obtained from the histograms.

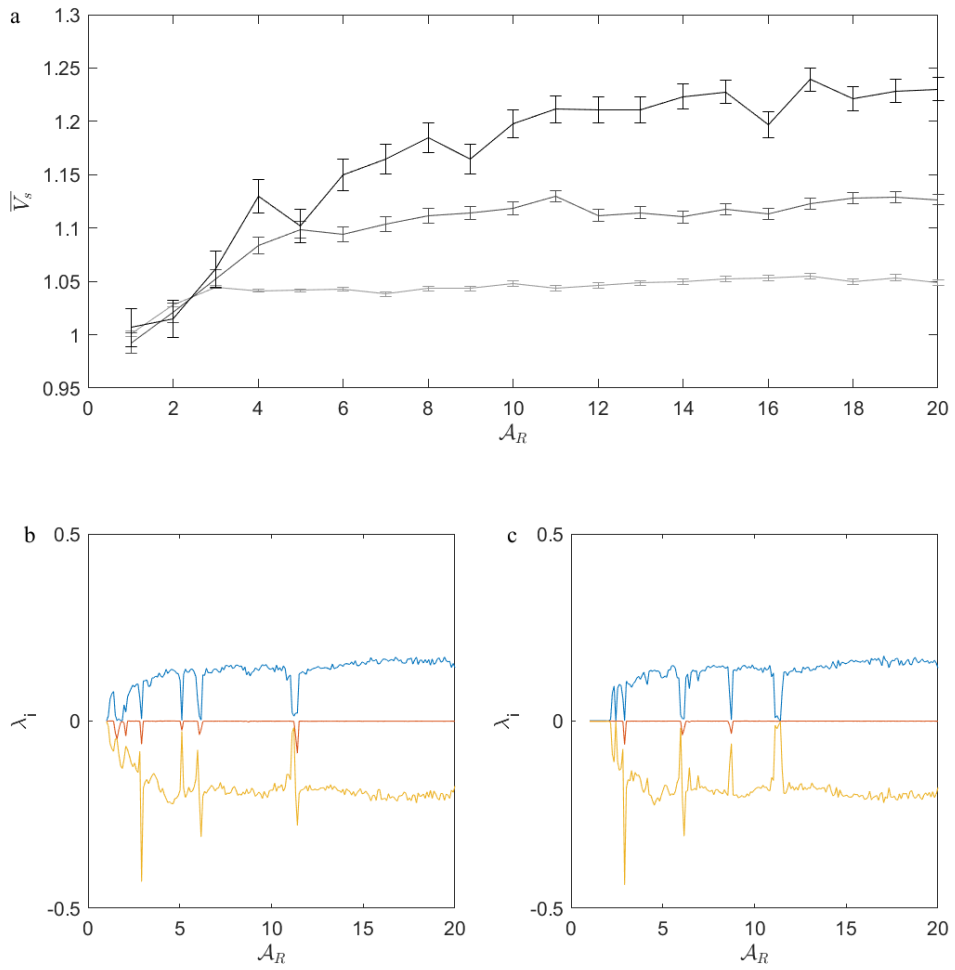

FIG. 11. (a) Average sedimentation speed, $\overline{V_s}$ as a function of aspect ratio, $\mathscr{A}_R$ for shear rate $\gamma = 0.5$ (light grey), $\gamma = 1$ (dark grey), and $\gamma = 1.5$ (black). Numerical simulations performed in cellular flow with $N = 1000$ particles, duration $T(\gamma, \mathscr{A}_R)$, with x_0, y_0 and θ_0 randomly sampled from $U(0, 2\pi)$. (b,c) Long-time Lyapunov exponents with initial conditions $(x_0, y_0, \theta_0) = (0,0,0)$ (b), and $= (5, \pi, 0)$ (c).

evance in the context of the formation of thin layers of plankton, we also identified that in horizontal Kolomogorov flow, particles can aggregate in horizontal layers associated with high shear because of shear-dependent sedimentation speed. This has previously been studied for swimming cells (e.g. Santamaria et al., 2014), but here we have presented a new mechanism for the formation of thin layers for non-motile, sedimenting particles. For cellular flow we explored the sedimentation speed of spheroidal particles and showed how spatially projected trajectories can intersect and give rise to chaotic dynamics for sufficiently large particle aspect ratio and rate of shear, to complement earlier studies on the persistence of Stommel retention zones (Mallier & Maxey, 1991; Shin & Maxey, 1997). In a similar manner to Kolmogorov flow we show that the mean sedimentation speed increases with aspect ratio and shear strength, with a concomitant accumulation of particles in down-welling regions.

There are some immediate extensions of this work. Without resorting to overcomplication, it would be useful to explore sedimentation dynamics associated with a time-dependent flow. A simple model would be Couette or Kolmogorov flow with a time-dependent shear rate. One might expect there to be resonances between the reorientation of the particle and time scales associated with changes to the flow. For time-dependent Couette flow the results may reflect the mechanisms associated with the steady Kolmogorov case. Alternatively, a weak time-dependent transverse flow may be imposed, such as the shear investigated in (Bees et al., 1998b) for Langmuir circulation. In a similar manner, and as a simple model of turbulence, it would be revealing to explore sedimentation dynamics in a three-dimensional, chaotic flow, such as the ABC model (Gromeka, 1881). Furthermore the three-dimensional orientation of particles should also be considered, as this can lead to very different predictions on the impact of flow on sedimenting speed even for simple two-dimensional flow fields. For example, if a particle was aligned with the direction of the vorticity in either of the simple Couette flow fields considered here, then the particle would maintain this orientation, and the settling speed would not be modified due to the mechanisms discussed here.

As commented above, the results draw a parallel with those of Zöttl & Stark (2012, 2013) for swimming cells, which depending on the geometry, initial conditions and parameters can swing across Poiseuille flow or tumble with periodic or quasiperiodic motion. It would be useful to explore sedimentation in axisymmetric shear flows and also to allow for the slow swimming of settling phytoplankton. In our model, we have assumed throughout that particles are advected at the local fluid velocity, and sink with a settling velocity dependent on orientation. The framework developed by Maxey & Riley (1983) and extended to nonspherical particles (Maxey, 1990) provides a more complete description to investigate the role of inertia and finite-size effects. Investigating this more fully, and determining when and how particles deviate from our model assumptions, particularly in the long-term Lagrangian statistics (Ouellette et al., 2008), could provide further insight into the 'real-world' relevance of our results.

The role of rotational diffusion may be important for small phytoplankton; both to represent small scale turbulent fluctuations and biological noise. This could be explored by developing stochastic differential equations for the orientation, or equivalently developing a Fokker-Planck equation for cell orientation. This approach has proved useful to gain insight into, for example, suspension rheology (Hinch & Leal, 1972) and the distribution of swimming cells (Pedley & Kessler, 1990; Bees et al., 1998a). More recent work has demonstrated the need to carefully consider the coupling between the spatial and orientation distribution of cells when calculating the transport and spatial distribution of swimming cells (Hill & Bees, 2002; Bearon et al., 2011, 2012). Applying these methods to elongated negatively buoyant particles would allow for an investigation of the impact of rotational diffusion.

Whilst the flows explored in this article appear somewhat distinct to those observed in the oceans, the individual phytoplankton are sufficiently small that they feel only the local shear. It is important to understand the individual responses to simple well-defined flow and the mechanisms for accumulation

and enhanced sedimentation that may result. This study goes some way towards this aim, but there are still many fascinating mechanisms yet to unveil.

5. Acknowledgment

We acknowledge support from EP/N032861/1 and, in particular, thank the SIG on Biologically Active Fluids, which organised a meeting in memory of John Blake in Birmingham in July 2017. We also acknowledge support from the COST Action MP1305: Flowing matter, which facilitated discussions relating to this article during the workshop 'Microorganisms in Turbulent Flows,' Lorentz Centre, Leiden, the Netherlands.

A. Appendix

From equation (3.6), we have that

$$V_s^{adv} = \frac{1}{T}\int_0^T -\gamma x dt. \tag{A.1}$$

For particles which undergo complete Jeffery orbits, we can make a change of variable in the integral from time, t, to orientation angle, θ, and use equation (3.4) for the angular velocity, to give this component of the sink speed as

$$V_s^{adv} = \frac{1}{T}\int_0^{2\pi} -\frac{2\gamma x}{\gamma(-1+\beta\cos 2\theta)} d\theta. \tag{A.2}$$

We then can make use of the expression for γx given by equation (3.7), to replace the integrand by a function of θ alone:

$$V_s^{adv} = \frac{1}{T}\int_0^{2\pi} -\frac{1}{\beta}\frac{s_r}{s_r+2}\ln\frac{1-\beta\cos 2\theta}{1-\beta\cos 2\theta_0}\frac{2}{\gamma(-1+\beta\cos 2\theta)} d\theta. \tag{A.3}$$

Finally, on inserting the expression for the duration of the orbit, T, given by equation (3.1), and simplifying, we obtain the required expression given in equation (3.8):

$$V_s^{adv} = -\frac{\sqrt{1-\beta^2}}{2\pi\beta}\frac{s_r}{s_r+2}\int_0^{2\pi}\frac{1}{1-\beta\cos 2\theta}\ln\frac{1-\beta\cos 2\theta}{1-\beta\cos 2\theta_0} d\theta. \tag{A.4}$$

From equation (3.6), we have that

$$V_s^{sed} = \frac{1}{T}\int_0^T \frac{2}{s_r+2}(s_r\cos^2\theta+1) dt. \tag{A.5}$$

Again, for particles which undergo complete Jeffery orbits, we can make a change of variable in the integral from time, t, to orientation angle, θ, and use equation (3.4) for the angular velocity, and equation (3.1) for the duration of the orbit, to give this component of the sink speed as

$$V_s^{sed} = \frac{\sqrt{1-\beta^2}}{\pi(s_r+2)}\int_0^{2\pi}\frac{s_r\cos^2\theta+1}{-1+\beta\cos 2\theta} d\theta. \tag{A.6}$$

On integration we obtain the expression given in equation (3.8):

$$V_s^{sed} = 1 + \frac{s_r}{\beta(s_r+2)}\left(1-\sqrt{1-\beta^2}\right). \tag{A.7}$$

REFERENCES

Angilella, J.-R. (2007) Asymptotic analysis of chaotic particle sedimentation and trapping in the vicinity of a vertical upward streamline. *Phys. Fluids*, **19**(7), 073302.

Ardekani, M. N., Sardina, G., Brandt, L., Karp-Boss, L., Bearon, R. N. & Variano, E. A. (2017) Sedimentation of inertia-less prolate spheroids in homogenous isotropic turbulence with application to non-motile phytoplankton. *J. Fluid Mech.*, **831**, 655–674.

Bearon, R. N., Bees, M. A. & Croze, O. A. (2012) Biased swimming cells do not disperse in pipes as tracers: A population model based on microscale behaviour. *Phys. Fluids*, **24**(12).

Bearon, R. N. & Hazel, A. L. (2015) The trapping in high-shear regions of slender bacteria undergoing chemotaxis in a channel. *J. Fluid Mech.*, **771**.

Bearon, R. N., Hazel, A. L. & Thorn, G. J. (2011) The spatial distribution of gyrotactic swimming micro-organisms in laminar flow fields. *J. Fluid Mech.*, **680**, 602–635.

Bees, M. A., Hill, N. A. & Pedley, T. J. (1998a) Analytical approximations for the orientation distribution of small dipolar particles in steady shear flows. *J. Math. Biol.*, **36**(3), 269 – 298.

Bees, M. A., Mezic, I. & McGlade, J. (1998b) Planktonic interactions and chaotic advection in Langmuir circulation. *Math. Comput. Simul.*, **44**(6), 527–544.

Bergougnoux, L., Bouchet, G., Lopez, D. & Guazzelli, É. (2014) The motion of solid spherical particles falling in a cellular flow field at low Stokes number. *Phys. Fluids*, **26**(9), 093302.

Durham, W. M., Climent, E., Barry, M., Lillo, F. D., Boffetta, G., Cencini, M. & Stocker, R. (2013) Turbulence drives microscale patches of motile phytoplankton. *Nature Comm.*, **4**, 2148.

Durham, W. M., Kessler, J. O. & Stocker, R. (2009) Disruption of vertical motility by shear triggers formation of thin phytoplankton layers. *Science*, **323**(5), 1067–70.

Gromeka, I. (1881) Some cases of incompressible fluid motion. *Scientific notes of the Kazan University*, pages 76–148.

Guazzelli, É. & Hinch, J. (2011) Fluctuations and Instability in Sedimentation. *Ann. Rev. Fluid Mech.*, **43**(1), 97–116.

Hill, N. A. & Bees, M. A. (2002) Taylor dispersion of gyrotactic swimming micro-organisms in a linear flow. *Phys. Fluids*, **14**(8), 2598 – 2605.

Hillary, R. M. (2003) *Effects of turbulence and a patchy environment on the dynamics of plankton populations.* PhD thesis, University of Surrey.

Hinch, E. J. & Leal, L. G. (1972) Effect of Brownian motion on rheological properties of a suspension of non-spherical particles. *J. Fluid Mech.*, **52**, 683–712.

Hojman, S. A. (2015) Construction of Lagrangian and Hamiltonian structures starting from one constant of motion. *Acta Mechanica*, **226**(3), 735–744.

Hope, A., Croze, O., Poon, W., Bees, M. A. & Haw, M. (2016) Resonant alignment of microswimmer trajectories in oscillatory shear flows. *Phys. Rev. Fluids*, **1**, 1–8.

Jeffery, G. B. (1922) The Motion of Ellipsoidal Particles Immersed in a Viscous Fluid. *Proc. Roy. Soc. London Ser. A*, **102**(715), 161–179.

Kessler, J. O. (1985) Hydrodynamic focusing of motile algal cells. *Nature*, **313**(5999), 218–220. 10.1038/313218a0.

Kim, S. & Karrila, S. J. (2005) *Microhydrodynamics: Principles and Selected Applications*. Dover Publications Inc.

Mallier, R. & Maxey, M. (1991) The settling of nonspherical particles in a cellular flow field. *Phys. Fluids A*, **3**(6), 1481–1494.

Margalef, R. (1978) Life-forms of phytoplankton as survival alternatives in an unstable environment. *Oceanol. Acta,*, **1**, 493–509.

Maxey, M. R. (1990) On the advection of spherical and nonspherical particles in a nonuniform flow.. *Phil. Trans. R. Soc. (London) A*, **333**, 289–307.

Maxey, M. R. & Riley, J. J. (1983) Equation of motion for a small rigid sphere in a nonuniform flow. *Phys. Fluids*, **26**, 883–889.

O'Malley, S. & Bees, M. A. (2012) The orientation of swimming biflagellates in shear flows. *Bull. Math. Biol.*, **74**(1), 232–55.

Ouellette, N. T., O'Malley, P. J. J. & Gollub, J. P. (2008) Transport of Finite Sized Particles in Chaotic Flow. *Phys.l Rev. Letts.*, **101**, 174504.

Pedley, T. J. & Kessler, J. O. (1990) A new continuum model for suspensions of gyrotactic microorganisms. *J. Fluid. Mech.*, **212**, 155 – 182.

Ruiz, J., Macías, D. & Peters, F. (2004) Turbulence increases the average settling velocity of phytoplankton cells. *Proc. Natl. Acad. Sci. USA*, **101**(51), 17720–17724.

Rusconi, R., Guasto, J. S. & Stocker, R. (2014) Bacterial transport suppressed by fluid shear. *Nature Phys.*, **10**(3), 212–217.

Santamaria, F., De Lillo, F., Cencini, M. & Boffetta, G. (2014) Gyrotactic trapping in laminar and turbulent Kolmogorov flow. *Phys. Fluids*, **26**(11), 111901.

Shin, H. & Maxey, M. R. (1997) The chaotic motion of nonspherical particles settling in a cellular flow field. *Phys. Rev. E*, **56**, 5431–5444.

Siewert, C., Kunnen, R. P. J., Meinke, M. & Schröder, W. (2014) Orientation statistics and settling velocity of ellipsoids in decaying turbulence. *Atmospheric Research*, **142**(Supplement C), 45–56. The 16th International Conference on Clouds and Precipitation.

Smayda, T. J. (1970) The suspension and sinking of phytoplankton in the sea. *Oceanogr. Mar. Biol. Annu. Rev.*, **8**, 353–414.

Stommel, H. (1949) Trajectories of small bodies sinking slowly through convection cells. *J. Mar. Res.*, **8**, 249–276.

Torney, C. & Neufeld, Z. (2007) Transport and Aggregation of Self-Propelled Particles in Fluid Flows. *Phys. Rev. Lett.*, **99**, 078101.

Voth, G. A. & Soldati, A. (2017) Anisotropic Particles in Turbulence. *Ann. Rev. Fluid Mech.*, **49**(1), 249–276.

Wang, L.-P. & Maxey, M. R. (1993) Settling velocity and concentration distribution of heavy particles in homogeneous isotropic turbulence. *J. Fluid Mech.*, **256**, 27–68.

Zöttl, A. & Stark, H. (2012) Nonlinear Dynamics of a Microswimmer in Poiseuille Flow. *Phys. Rev. Lett.*, **108**, 218104.

Zöttl, A. & Stark, H. (2013) Periodic and quasiperiodic motion of an elongated microswimmer in Poiseuille flow. *European Phys. J. E*, **36**(1), 4.